Thermal characterization of Ge-rich GST thin films for phase change memories by Raman thermometry

Akash Patil, Yannick Le-Friec, Pascal Roussel, Yves Deblock, Simon Jeannot, Philippe Boivin, Emmanuel Dubois, Jean-François Robillard

Journal of Applied Physics

RESEARCH ARTICLE | NOVEMBER 01 2024

Thermal characterization of Ge-rich GST thin films for phase change memories by Raman thermometry

Special Collection: Phase-change Materials and Their Applications

Akash Patil ; Yannick Le-Friec ; Pascal Roussel ; Yves Deblock ; Simon Jeannot; Philippe Boivin ; Emmanuel Dubois ; Jean-François Robillard

J. Appl. Phys. 136, 175102 (2024)
https://doi.org/10.1063/5.0226265

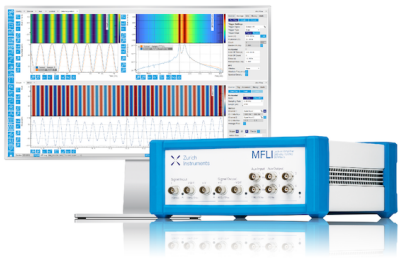

AIP Publishing

Journal of Applied Physics ARTICLE pubs.aip.org/aip/jap

Thermal characterization of Ge-rich GST thin films for phase change memories by Raman thermometry

Cite as: J. Appl. Phys. **136**, 175102 (2024); doi: 10.1063/5.0226265
Submitted: 30 June 2024 · Accepted: 9 October 2024 ·
Published Online: 1 November 2024

Akash Patil,[1,2] Yannick Le-Friec,[2] Pascal Roussel,[3] Yves Deblock,[1] Simon Jeannot,[2] Philippe Boivin,[4] Emmanuel Dubois,[1] and Jean-François Robillard[1,a)]

AFFILIATIONS

[1]Univ. Lille, CNRS, Univ. Polytechnique Hauts-de-France, Junia, UMR 8520—IEMN—Institut d'Electronique de Microélectronique et de Nanotechnologie, F-59000 Lille, France
[2]STMicroelectronics, 850 rue jean Monnet 38920 Crolles, France
[3]Univ. Lille, CNRS, ENSCL, Centrale Lille, Univ. Artois, UMR 8181—UCCS—Unité de Catalyse et de Chimie du Solide, F-59000 Lille, France
[4]STMicroelectronics, 190 avenue Coq, 13106 Rousset, France

Note: This paper is part of the special topic, Phase-change Materials and Their Applications.
[a)]**Author to whom correspondence should be addressed:** jean-francois.robillard@iemn.fr

ABSTRACT

Doped GeSbTe (GST)-based phase change materials are of growing interest due to their ability to enable high-temperature data retention for embedded memory applications. This functionality is achieved through Ge enrichment and addition of dopants such as N and C in stoichiometries such as GST-225, which improve the crystallization temperature and thermal phase stability. In this study, we examine the effect of these dopants on thermal conductivity using Raman thermometry. We report the temperature-dependent thermal conductivity of the amorphous and crystalline phases of Ge-rich GeSbTe (GGST) and Ge-rich GeSbTe N-doped (GGSTN) thin films. The results reveal a surprising temperature dependence of the thermal conductivity of the crystalline phase of GGST and GGSTN, a phenomenon not typically observed for GST-based materials. Additionally, enrichment of Ge and subsequent N-doping result in reduced thermal conductivity, which can benefit the power consumption of phase change memories. From a characterization perspective, Raman thermometry has been developed as a technique for simultaneous structural and thermal characterization of GST-based materials.

I. INTRODUCTION

Phase change memories (PCMs) are enabled by the unique behavior of GeSbTe (GST)-based chalcogenide materials, which can reversibly switch between amorphous and crystalline phases with high resistivity contrast.[1–3] These two resistive states enable data storage in localized phase-changing volumes of the layered material. Among the emerging non-volatile memories (NVMs), PCM stands out as one of the most mature candidates owing to its excellent cycling endurance, good scalability, and low power consumption.[4,5] This is evidenced by its recent commercial realization for both, stand-alone and embedded memory applications.[6,7]

Materials engineering has played a crucial role in the realization of PCM as a viable technology. The flag-ship chalcogenide alloy $Ge_2Sb_2Te_5$ (GST-225) inherited from optical data storage paved the way for early development of PCM, as it showed nanosecond switching times between the two material phases.[8] However for potential NVM applications, GST-225 had several drawbacks such as low crystallization temperature (150 °C) that limited data retention, poor material reliability, and slow crystallization speed.[9,10] For NVMs, especially embedded memory applications, higher crystallization temperatures are essential to ensure high-temperature data retention.[11] From an integration point of view, PCMs embedded in the back-end-of-line (BEOL) should resist the

thermal budget of around 400 °C.[12] Also, it is crucial to guarantee data retention after solder reflow of 2 min at 260 °C to preserve the code. These requirements impose a stringent guideline for the development of phase change materials.

In this context, extensive materials engineering has been carried out in the last decade. Specifically, two routes were followed: compositional tuning of GST away from the pseudo-binary line of $GeTe–Sb_2Te_3$ toward Ge enrichment and further alloying of these stoichiometries with nitrogen or carbon.[13–15] An increase in the number of Ge–Ge bonds resulted in an increase in the crystallization temperature. Furthermore, the formation of Ge–N bonds retarded crystallization kinetics, which partially resolved the persistent issue of Ge segregation and controlled the grain size.[16,17] This sufficed the material requirements for high-temperature tolerance and control over grain size resulted in improved material reliability, which was lacking for GST-225. Stoichiometries such as Ge-rich N-doped GST-212 and GST-225 Ge45%–N4% doping displayed improved data retention, with the capability of 10 years at 210 °C for the later stoichiometry.[12,14] Ge-rich GST-doped alloys have become the material of choice for high-temperature embedded memory applications.

In PCMs, the reversible switching between phases is thermally initiated. Studies report that <1% of energy is utilized for phase change, whereas most of the energy is lost via other heat dissipation pathways in the PCM cell.[18] Here, thermal conductivity is a key physical parameter to understand the temperature distribution in the device and optimize the operation of a PCM device and cross-talk between cells. Therefore, knowledge of the thermal properties of phases over the entire operation temperature range of PCM cells is crucial. The flag-ship GST-225 alloy has been extensively characterized by various techniques,[19–28] but the current state-of-art falls short of thermal characterization of the newly engineered stoichiometries. From a characterization point of view, it is also crucial to have simultaneous thermal and physiochemical characterization of phase change materials.[29] Raman thermometry as a contactless characterization technique requiring no microfabrication provides this unique dual characteristic.

In this article, we implement Raman thermometry for the thermal characterization of Ge-rich GST and Ge-rich N-doped alloys for the first time. After a detailed explanation of the method, we demonstrate the successful extraction of temperature and phase-dependent thermal properties of these materials up to higher temperatures (~350 °C) by Raman thermometry for the first time. The study is supplemented by x-ray diffraction analysis, which agrees with the significant structural changes observed in Raman spectroscopy analysis, confirming the additional benefit of this technique.

II. EXPERIMENTAL DETAILS

A. Samples

Ge-rich GST (GGST) and Ge-rich GST N-doped (GGSTN) 200 nm thin films were deposited by physical vapor deposition on 300 mm silicon (100) wafers using an industrial tool. The Ge content of both these materials is greater than 45%. The thin films were capped right after deposition by a 45 nm silicon nitride thin film or a 10 nm titanium nitride to avoid oxidation. These capping materials were chosen as those are the preferred interfacing materials to GST in a phase change memory cell. Raman thermometry permits the choice of such capping materials.

The silicon nitride thickness was chosen to be 45 nm to optimize power absorption at a wavelength of 473.11 nm. This was evaluated by calculating the coefficients of reflection and absorption of the laser using the transfer matrix formalism. The calculation was performed iteratively from 0 to 150 nm of SiN thickness as presented in Fig. 1. The refractive index used for SiN and GST were extracted from the literature.[30–32] Figure 1 shows that the maximum laser power absorbed in amorphous GST is for SiN thickness ranging from 40 to 50 nm. Maximum absorption of laser light for different stoichiometries of chalcogenides in its amorphous and crystalline phase lies in the same range as shown in Fig. 2. This calculation was performed based on refractive index values from the literature for a general understanding of absorbance of laser light in GST to evaluate the SiN thickness for various GST-based stoichiometries. So, deposition of SiN thickness of 45 nm was chosen to maximize laser absorption. Furthermore, the absorbance of laser in GGST and GGSTN was confirmed by reflectometry as listed in Table S1 in the supplementary material. This configuration of thickness assures maximum laser power absorbed in GST for optimum Raman signal.

The samples were crystallized by annealing *ex situ* at 400 °C for 30 min at a heating rate of 0.5 °C/s under N_2 atmosphere. For thermal characterization, these samples were heated *in situ* at the respective temperatures under vacuum. At each temperature step, 5 min of thermalization of samples is performed, and each acquisition is performed after ensuring stable temperature and pressure conditions.

B. Raman thermometry setup

Raman spectroscopy and thermometry measurements were performed using a LabRAM HR confocal system from Horiba

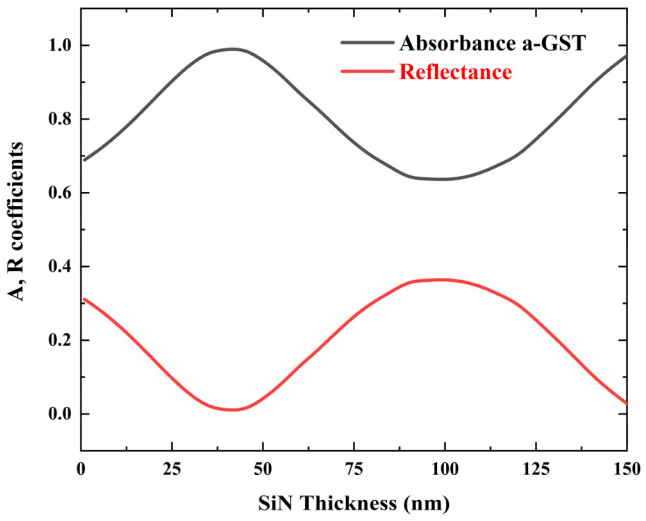

FIG. 1. Absorption and reflection coefficients of 473.15 nm laser in a stack with varying SiN_x thickness and GST thickness fixed at 200 nm.

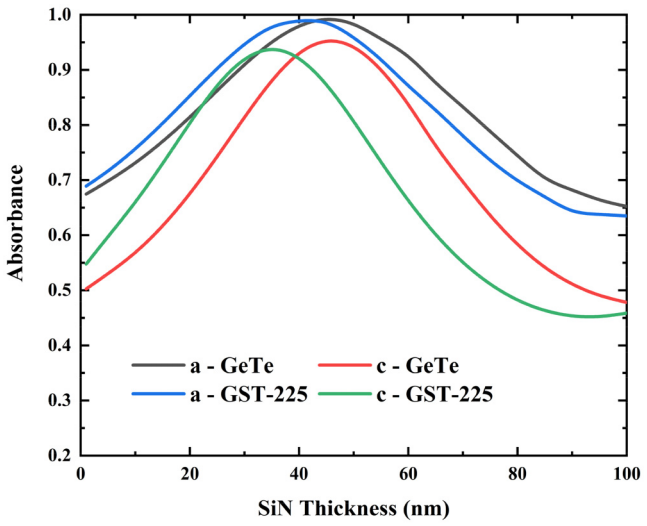

FIG. 2. Absorption coefficient of 473.15 nm laser in amorphous and crystalline phases of GeTe and GST-225 with varying SiN thickness.

Jobin-Yvon as illustrated in Fig. 3. The system is equipped with a continuous wave diode-pumped laser (473.11 nm) and 50× and 100× Mitutoyo Apochromatic NIR objectives. The features of the confocal system to ensure this high spectral resolution to resolve peaks are a spectrometer with a focal length of 800 mm, diffraction grating with 1800 grooves/mm, and spectral resolution at 473.11 nm < 0.7 cm^{-1}. This setup is modified with a continuously variable reflective neutral density filter—THORLABS NDL-25C-4 to enable control of the excitation laser intensity. For sample temperature control, a LINKAM heating stage—LINKAM HFS350-PB4 (−195 to 350 °C, vacuum compatible, liquid nitrogen cooling) with an optical window is used.

C. X-ray diffraction measurements

X-ray powder diffraction (XRD) was performed on a 9 kW rotated anode Rigaku Smartlab diffractometer working in a Bragg–Brentano geometry using Cu Kα radiation (λ = 1.5418 Å), equipped with a 2D Hypix Detector detector. To avoid saturation of the detector by the (004) peak of the single-crystal silicon substrate, after having verified that possible texture effects were negligible, a 2° misorientation was applied to the sample. Patterns were collected both at room temperature, on *ex situ* pristine and annealed samples, and *in situ* during heating. Taking advantage of the high flux of the x-ray beam delivered by the rotated anode and of the high sensitivity, of the 2D detector, patterns were acquired on the fly every 5 °C (heating from RT to 600 °C at 2 °C/min). The EVA 6.1, 2023, Bruker AXS GmbH, Karlsruhe, Germany software was used for phase identification.

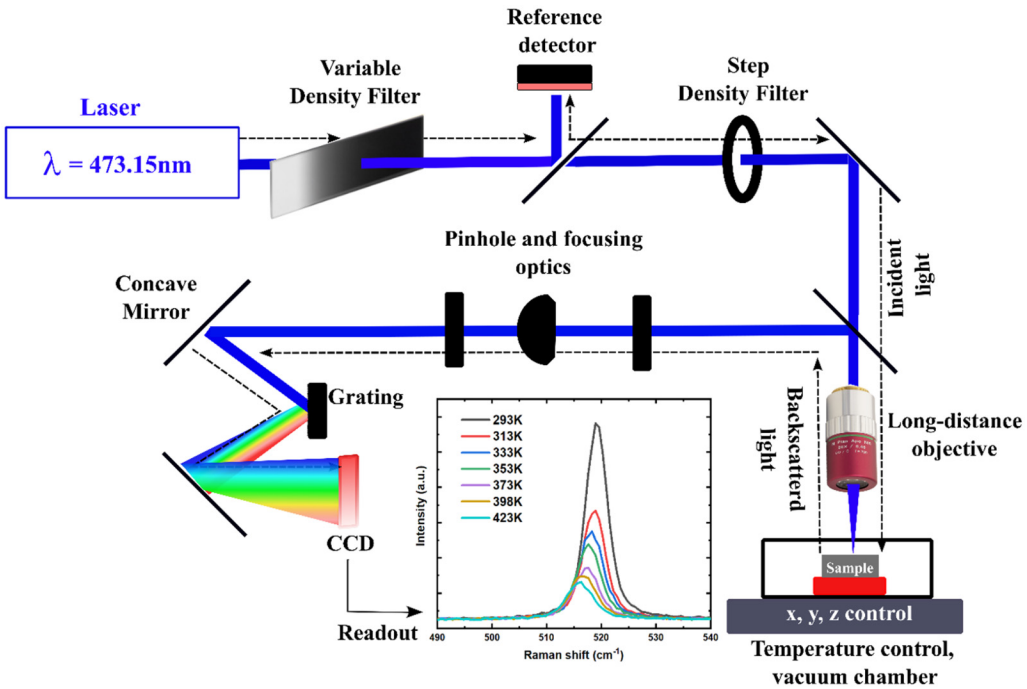

FIG. 3. Schematic of the Raman setup from Horiba Jobin-Yvon with the dotted light presenting the path of laser.

III. METHODOLOGY

A. Temperature calibration coefficients

Raman thermometry is a steady-state thermal characterization technique that leverages the temperature sensitivity of a Raman scattering peak as a local thermometer. It is a non-destructive optical method that provides sub-micrometer spatial resolution, requires no microfabrication, and offers high material selectivity as its key advantages over other thermal characterization techniques. This technique has been extensively used for semiconductors such as Si,[33] GaN,[34,35] graphene,[36] etc. but has not yet been implemented for chalcogenides. The essential material requirements for probing a material using Raman thermometry are (a) the material must be Raman active—meaning that it should produce a significant vibrational signature in the Raman spectra from one of its optical modes and (b) the vibrational modes should be sensitive to temperature.

To analyze the vibrational modes, present in GGST, Fig. 4 illustrates the Raman spectrum of as-deposited GGST with a Lorentzian fit to extract the precise peak position. The spectra can be categorized into Sb–Te, Ge–Te, and Ge–Ge vibrations. Spectra were acquired at a very low incident power (0.5 mW) to avoid any structural modifications. The acquisition time and averaging of a spectrum were optimized for signal-to-noise ratio by trial and error.

The most intense peak (B1) in GGST at ~158 cm^{-1} can be attributed to the stretching mode of Sb–Te vibrations in $SbTe_3$ pyramidal units.[37,38] This is similar to the case of Sb_2Te_3 and GST-225, where the presence of Sb–Te vibrations was evident due to its high polarizability.

In the low-frequency range, a significant peak A1 and a minor peak A2 are evident, one around 100 cm^{-1} and a second minor peak at 130 cm^{-1}. The first can be assigned to a contribution arising from both, Te–Te stretching mode or Ge–Te stretching mode at 90 and 110 cm^{-1}, respectively. The band at 130 cm^{-1} associates with the symmetric stretching of Ge–Te vibrations in $GeTe_{4-n}Ge_n$ (n = 1,2) corner-sharing units.[39–41] The vibrations observed in GGST arise from the bonds in a distorted octahedral arrangement, like in GST-225.

In the high-frequency range, peaks related to Ge in tetrahedral units are present. Peak A3 is assigned to Ge–Te vibrations in $GeTe_4$ tetrahedral units at 217 cm^{-1}. This peak can be considered as a convolution arising from a LO-like (longitudinal optic) at 222 cm^{-1}. Peak A4 at 272 cm^{-1} is assigned to the TO-like (transverse optic) mode of amorphous Ge.[42,43] The appearance of this peak confirms the presence of excess Ge and assures the amorphous nature of the material.

Figure 5 presents the Raman spectrum of GGST annealed at 400 °C for 30 min. Such annealing conditions are chosen in correspondence to the maximum thermal budget experienced by the PCM during BEOL integration. Due to crystallization, the TO-like (transverse optic) mode of amorphous Ge (A4 peak) transitions to a crystalline Ge tetrahedral peak at 299 cm^{-1}.[42] The Sb–Te peak shows a minor shift toward higher wavenumbers. Other peaks related to Ge–Te show minor rearrangement. The presence of Ge–Ge vibrations and GST matrix combined with Ge–Te and Sb–Te vibrations hints toward the formation of GST and Ge crystal grains. Sb–Te and Ge–Ge vibrational modes are the most intense and narrow peaks in both phases.

The next step is to analyze the temperature dependence of these vibrational modes. The Raman excitation laser beam is focused on the sample's surface. Since the sample is studied under vacuum and more importantly has a relatively low thermal

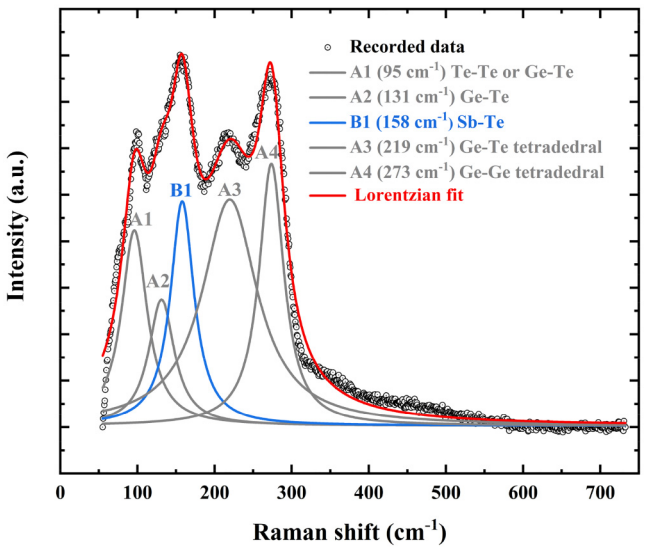

FIG. 4. Fitted Raman spectrum of as-deposited amorphous GGST is presented in a range of 50–750 cm^{-1}, the inset of the graphs denotes the vibrations responsible for the peaks.

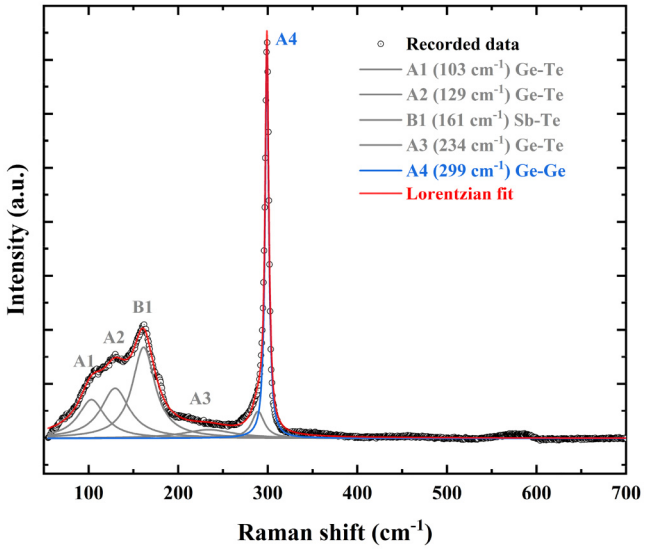

FIG. 5. Fitted Raman spectrum of crystalline-annealed (400 °C for 30 min) GGST is presented in a range of 50–750 cm^{-1}, the inset of the graphs denotes the vibrations responsible for the peaks.

conductivity, the input power induces a local temperature rise T_H–T_0. Here, T_H denotes the local temperature of the hot spot and T_0 is the sample stage temperature. The sensitivity of the spectral features of Raman peaks acts as the local thermometers providing the local temperature T_H based on the Raman peak shift observed.

First, a calibration of the material is performed to extract the temperature-dependent shift of the Raman peaks. This calibration is performed by changing the sample temperature T_0 while using very low laser power to avoid local heating and local structural changes. The temperature was ramped up at 20 °C/min and at every step a 5 min of thermalization period was maintained to ensure stable temperature and vacuum conditions. Figure 6 shows such calibration curves ($\omega_T = d\omega/dT$) for amorphous and crystalline GGST, which gives the calibration coefficient (ω_T) indicating the change in Raman shift (frequency—dω) with respect to temperature (dT).

The Raman spectrum was acquired at each temperature step and followed by the Lorentzian fitting procedure. The Raman shift of all the vibrational modes was analyzed as a function of temperature. The most temperature-sensitive peaks, Sb–Te and c-Ge–Ge, were chosen as "local thermometers." They also feature the highest intensity and lowest uncertainty in the peak position. Calibration coefficients for all the materials were analyzed as listed in Table S1 in the supplementary material.

B. Power-dependent measurements

Similarly, the change in the spectral peak position as a function of increasing laser power is recorded as ($\omega_P = d\omega/dP_{abs}$). This coefficient, ($\omega_P$), gives the change in Raman shift (frequency—dω) with respect to power absorbed in the GGST. P_{abs} is defined as P_{in}*A, where A is the absorbance of the material. The input power (P_{in}) was varied, and the material was held at constant stage temperature T_0. Figure 7 presents the change in Raman shift with increasing power (red axis) for varying stage temperatures. The continuous density filter was used to vary the input power and was regulated by power measurements.

Thus, an increasing $\Delta T = T_H - T_0$ is induced between the hot spot and the sample boundaries, as indicated in Fig. 7. Generally speaking, it is then possible to extract the effective thermal conductance (G) of the stack as the ratio of temperature and power-related coefficients defined as

$$G = \frac{\frac{d\omega}{dT}}{\frac{d\omega}{dP_{abs}}} = \frac{\Delta P_\omega}{\Delta T_\omega} \quad \left[\frac{W}{K}\right]. \tag{1}$$

It should be noted that this quantity encompasses all the stack thermal properties in geometry, not only the layer of interest. This experimental process is repeated by ramping up the stage temperature and analyzing the material's power dependence as presented in Fig. 7. In this way, temperature dependence of thermal conductance can be extracted.

C. Finite element model

In order to quantitatively extract the GGST thermal conductivity (κ_{GGST}) from G, a model must be used in order to establish an abacus of G(κ_{GGST}). The analytical solution of the laser-induced

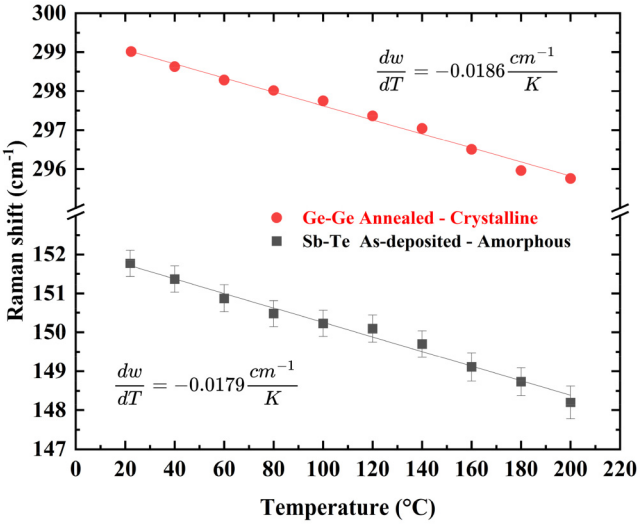

FIG. 6. Temperature calibration curve of the Sb-Te phonon mode of as-deposited amorphous GGST and c-Ge phonon mode of annealed crystalline GGST. Inset values denote the calibration coefficients of these thermometers.

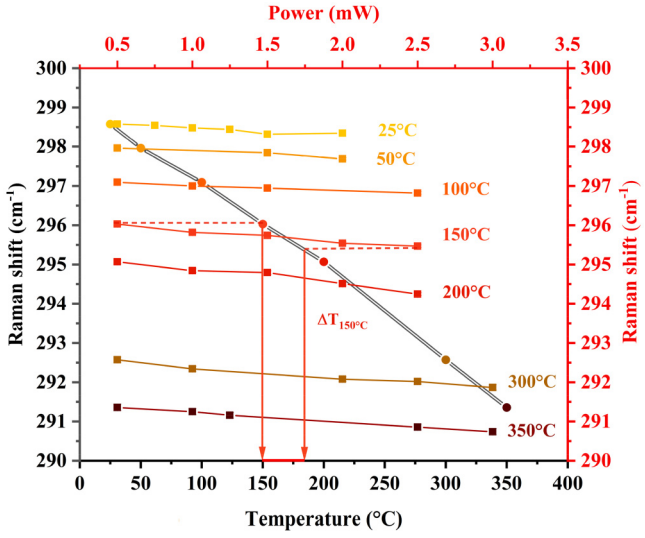

FIG. 7. Temperature calibration plot (black axes) with data points connected by double black lines and power calibration plot (red axes), where the colored data points are connected by colored lines (color gradient representing the respective temperature). The power calibration colored data points at 0.5 mW align with the temperature calibration data points along the black line. A representative example of local temperature rise caused by a 2.5 mW input power for an *in situ* measurement performed at 150 °C.

local heating in a semi-infinite medium is well-known.[44,45] In the case of a multilayered thin film, an analytical solution is cumbersome, thus, a finite element model (FEM) was built to quantify the heat transfer in the system induced by the Raman laser beam in COMSOL Multiphysics®. The problem is axisymmetric, and the material properties are modeled locally dependent on the temperature. Here, the thermal conductivity of GGST (κ_{GGST}) is parametrized and thermal conductance is extracted as a function of κ_{GGST}. Temperature-dependent thermal properties are defined for the materials and interfaces. These properties are defined for the relevant thicknesses as SiN[46] and TiN[47] show thickness dependence. For thermal boundary resistance, the values are identified for SiN-GST-225 and[48] TiN-GGST[49] as available in the literature (listed in Table S2 in the supplementary material).

The heat source profile originating from a 100× NIR objective was defined as

$$P_{abs}(r)^{100x} = P_{in}A\left(\mu \exp\left(-\frac{r^2}{R_{w1}^2}\right) + (1-\mu)\exp\left(-\frac{r^2}{R_{w2}^2}\right)\right), \quad (2)$$

where $\mu = 0.55$, $R_{w1} = 0.56\,\mu m$, $R_{w2} = 8.9\,\mu m$, and A is the absorbance coefficient of laser power in GGST. The beam waist of the laser spot was evaluated by the knife-edge method. Two beam waists are necessary to correctly describe the focal profile from the 100× objective resulted as a contribution (μ) of two Gaussian beams.

The extraction of thermal conductivity is based on the Fourier law of heat conduction, $q = -\kappa \nabla T$ where q is the heat flux density, κ is the thermal conductivity, and ∇T is the temperature gradient. Now, the quantity to evaluate is the thermal conductance (G) of the stack as taken between the heat source defined above and the stage temperature. Here, the local temperature, i.e., the effective hotspot temperature is a function of the thermal conductivity, and the thermal conductance is defined as

$$G(\kappa) = \frac{P_{abs}}{T_H(\kappa) - T_{stage}}. \quad (3)$$

An important point here is to take into account the fact that (i) since the laser source is a Gaussian beam, T_H is not homogeneous over the focal spot area (supplementary material, Sec. S3). (ii) Second, since the local temperature is measured from the Raman signal, which itself originates from the integrated spectra collected from the Gaussian beam, the resulting hot temperature is defined as

$$T_H = \frac{1}{P_{abs}} \iint P(\vec{r})T(\vec{r})dS. \quad (4)$$

This provides a correlation between thermal conductance as a function of the thermal conductivity of GGST which can be extracted from the $G(\kappa_{GGST})$ abacus, as presented in Fig. 8.

IV. RESULTS

Figure 9 displays the thermal conductivity of amorphous, as-deposited, GGST, and GGSTN measured from room temperature to 200 °C. Study at higher temperatures was not possible due to local structural changes in these alloys which abnormally affected the position of the vibrational modes. The thermal conductivity lies between 0.25 and 0.35 $W\,m^{-1}\,K^{-1}$ in agreement with a

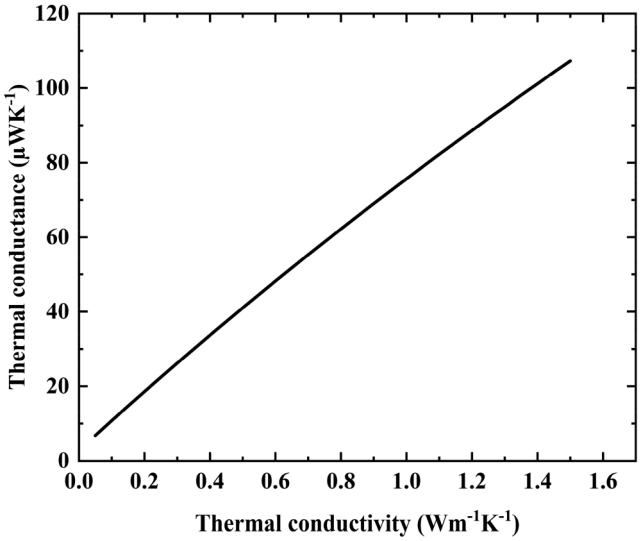

FIG. 8. Thermal conductance extracted as a function of thermal conductivity of GGST extracted from FEM.

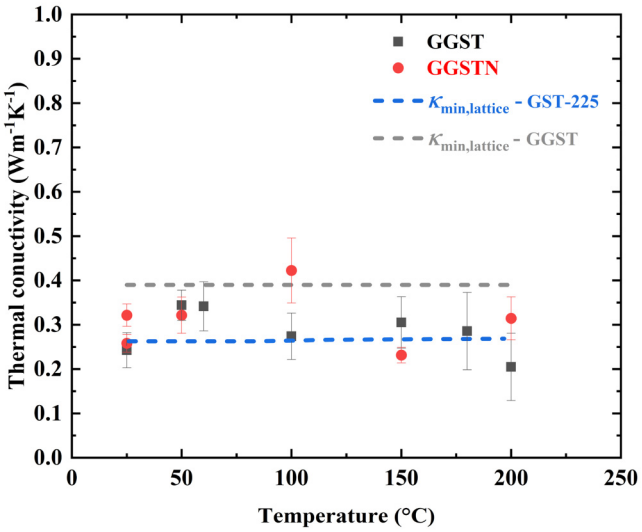

FIG. 9. Measured thermal conductivity as a function of temperature for GGST and GGSTN (both capped with SiN). Dashed lines present the min theoretical limit for lattice (phonon) contribution calculated using the Cahill–Pohl model for GST-225 and GGST parameters. The experimental values and minimum thermal conductivity law agree well. The longitudinal and transverse sound velocities are input for GST-225[20] are 2250 m/s, 1350 m/sand GGST[49] are 3600 and 2530 m/s, respectively.

prior measurement for GGST.[48] The values are similar to the amorphous phase thermal conductivity of most GST stoichiometries exhibiting very low thermal conductivity.[26] In amorphous materials, thermal transport is dictated by the vibrational component as the contribution due to electronic transport is almost negligible. For these amorphous solids, a lower limit of thermal conductivity, $k_{ph,min}$, is obtained from the Cahill–Pohl model where the thermal transport is assumed as a random walk of energy between neighboring oscillators.[50] This model is valid above the Debye temperature of the material defined as

$$k_{ph,min} = \frac{1}{2}\left(\frac{\pi}{6}\right)^{\frac{1}{3}} K_b n^{\frac{2}{3}} (v_l + 2v_t), \quad (5)$$

where n is the atomic density (3.09×10^{22} cm^{-3}),[20] υ_l and υ_t are the longitudinal and transverse sound velocities. As shown in Fig. 9, the two limits are assigned to the speed of sound calculated for GST-225 and GGST, respectively. The mean free path of phonons is extremely small (~5.2–7.6 Å)[26] and constant with temperature, indicating no thickness dependence of thermal conductivity. Ge enrichment and N-doping do not affect the thermal transport in amorphous GST. Overall, good agreement for the thermal conductivity as extracted from Raman thermometry is found with the theoretical lower limit calculations.

Next, the crystalline phase thermal conductivity study was conducted on pre-annealed samples. Note that, as Raman thermometry is a steady-state technique, dynamic evaluation of thermal conductivity from amorphous to crystalline is not possible, as in the case of other widely used techniques. Figure 10 displays the thermal conductivity of the pre-annealed–crystalline phases of GGST (with SiN capping) and GGSTN (with SiN and TiN capping) from room temperature to 350 °C. The measured thermal conductivity value of GGST at room temperature is 1.02 W m^{-1} K^{-1}, higher than GGSTN at 0.8 W m^{-1} K^{-1}. It is evident that N-doping affects the thermal conductivity by controlling crystallization and nucleation-growth kinetics.

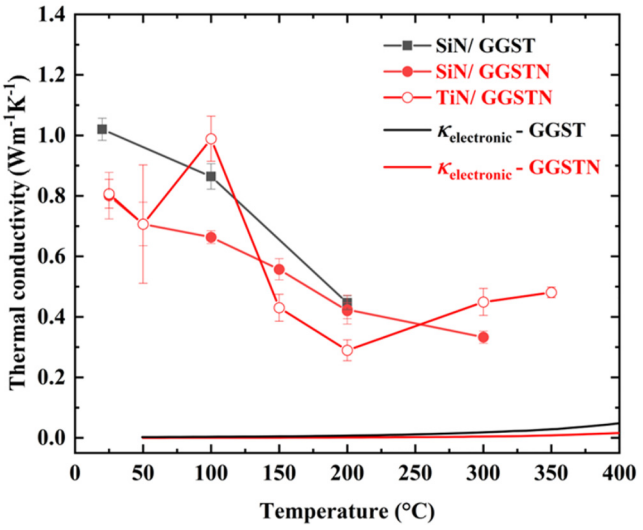

FIG. 10. Measured thermal conductivity as a function of temperature for c-GGST (capped with SiN) and c-GGST (capped with SiN and TiN) annealed at 400 °C for 30 min. The electronic contribution is calculated using the Wiedemann–Franz law by using the resistivity data presented for the respective thin. The contribution of electronic conductivity to the total thermal conductivity is negligible to affect the temperature dependence.

Next, thermal conductivity shows a temperature dependence which is contrary to the observations for GST-based materials. So, the contribution to thermal conductivity from its phonon and electron components is analyzed. Assuming that GGST behaves as a metal in its crystalline state, the electronic contribution is calculated by the Wiedemann–Franz law by using the resistivity data of the materials (listed in Fig. S1 in the supplementary material). The continuous lines shown in Fig. 10 show that the electronic contribution toward resistivity is quite low. Considering the entire range of Lorenz number from 1.5 to 2.44×10^{-8} W Ω K^{-2},[26] the electronic contribution at room temperature is negligible whereas at higher temperatures it is in the range of 2%–5%. This hints that the major contribution arises from the lattice contribution. So, the decreasing thermal conductivity behavior could be due to phonon scattering processes. As the temperature increases, the decreasing trend of κ for GGST and GGSTN is analogous to the behavior of highly crystalline solids. For temperatures above the one tenth of the Debye temperature, $T_D = \hbar \upsilon_s (6\pi n_a)^{1/3}/k_B$, κ decreases with increasing temperature due to the onset of the three phonon Umklapp scattering process. For GST alloys, the Debye temperature is estimated to be −18 °C for GST-124 and −53 °C for GST-225.[26,51] Estimating the Debye temperature of GGST for sound velocities $v_l = 3600$ m/s and $v_t = 2530$ m/s, results in T_D as −99 °C, which is well below the temperature range in consideration confirming the possibility of the Umklapp scattering process. This behavior of the alloys with temperature is reversible as the higher room temperature conductivity is attained on cooling back to room temperature.

For other GST alloys, mainly GST-225, extensive analysis shows that lattice contribution does show temperature dependence but is compensated with the increasing electronic contribution owing to the superior electrical conductivity, maintaining constant thermal conductivity.[20,25,27] This electrical conductivity is hampered in the case of GGST due to Ge doping by two to three orders of magnitude. For GGST, as the electronic contribution is low and the lattice component is the majority contributor to thermal conductivity, temperature dependence of the total thermal conductivity is evident.

Structural analysis of GST by XRD patterns shows sharp features of cubic Ge with trigonal GST (t-GST) and cubic-GST (c-GST) phases as shown in Fig. 11. For the same annealing conditions, GGSTN shows broad features with the presence of only cubic Ge and GST phases. This suggests that in GGST, the sharper peaks indicate the growth of the initially small grains, whereas in GGSTN, the grain size remains smaller. Evaluation of Ge grain size (peak Ge [111]) results in 28.96 and 7.35 nm for GGST and GGSTN, respectively. So, N-doping affects crystallization as it bonds primarily to Ge and controls the nature of the growth of crystals. Furthermore, it restricts the formation of a more ordered trigonal structure in GGSTN as is the case for GGST. Also, the thermal budget provided for GGSTN is not sufficient to obtain a

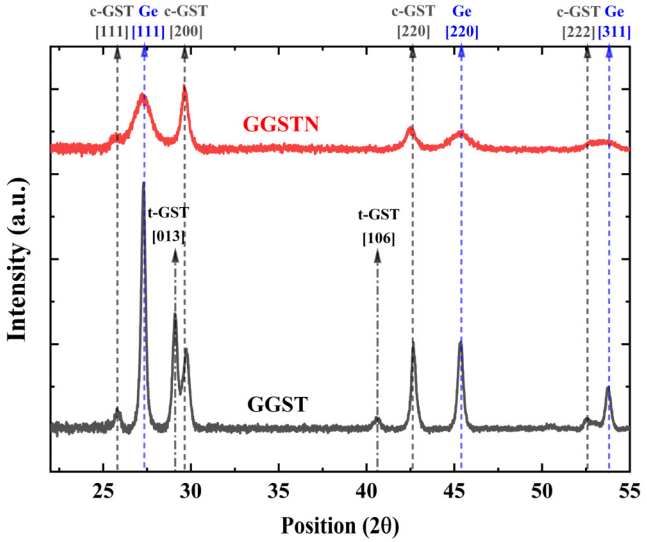

FIG. 11. Evolution for GGST and GGSTN for same annealing conditions—400 °C for 30 min. Impact of annealing conditions is evident with sharp peaks and presence of trigonal GST (t-GST) in GGST whereas only cubic-GST (c-GST) phases are present in GGSTN. PDF card information: c-Ge (00-004-0545), cubic-GST—GSTC (00-054-0484), trigonal GST—GSTT (89-2233).

material of higher crystallinity reflecting in the thermal conductivity differences.

Similar conclusions can be drawn from the Raman spectrum presented in Fig. 12, where the peak characteristics are broader for

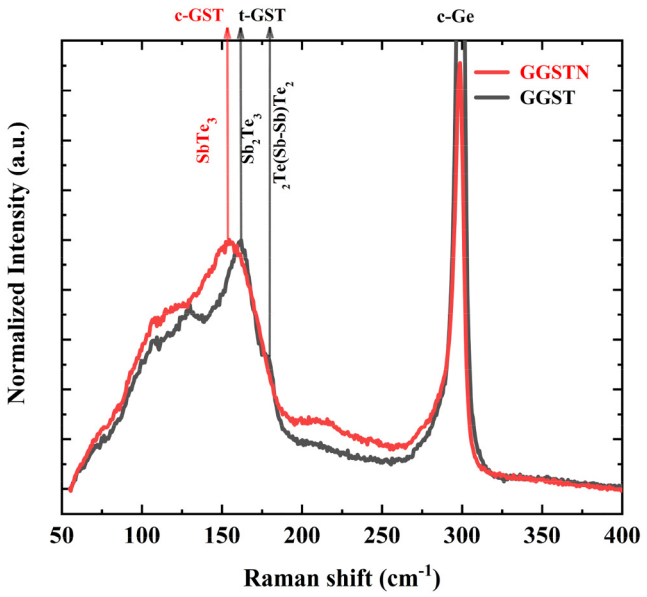

FIG. 12. Raman spectrum of GGST is characterized by sharper peaks and presence of Sb_2Te_3 vibrations signifying trigonal GST phase, whereas GGSTN has broader peaks for similar annealing conditions.

GGSTN. The Sb–Te peak characteristics indicate a difference in the structure of GGST and GGSTN. GGST has one sharp peak at 162 cm^{-1} and a shoulder at 175 cm^{-1} whereas GGSTN has a rather broad peak at 154 cm^{-1} as presented in Fig. 12. The shoulder arising at 175 cm^{-1} could be because of the vibrations from Sb–Sb bonds arising from $(Te_2)Sb–Sb(Te_2)$ units present at 174 cm^{-1}. This indicates a transition to a trigonal-like structure for GGST for these annealing conditions. On the contrary, for GGSTN, the Sb–Te vibrations move toward the $SbTe_3$ vibrations at 153 cm^{-1}. The Sb–Te vibrations arising from $SbTe_3$ in GGST or GGSTN are correlated to the cubic structure of GST. The presence of trigonal structural motifs and larger grain size contributes to the higher thermal conductivity of GGST. It is understood from this behavior that GGST transitions from amorphous to cubic and then to the trigonal phase, whereas the thermal budget implemented for GGSTN was not sufficient to foresee the transition to the trigonal phase. For GST alloys, trigonal structural features result in higher thermal conductivity rather than the cubic phase, and in general, for polycrystalline materials, grain size evidently affects thermal conductivity. Furthermore, a clear correlation between Raman and XRD results indicates the complementary structural analysis nature of Raman thermometry.

V. CONCLUSION

The thermal conductivity of Ge-rich GST and Ge-rich GST N-doped thin films has been reported using Raman thermometry. The amorphous phase thermal conductivity aligns well with the minimum thermal conductivity model and, the general expectation of thermal conductivity for GST-based alloys. In contrast, the room temperature thermal conductivity of crystalline phase drops from 1.5 $W\,m^{-1}\,K^{-1}$ of GST-225 to 1.02 $W\,m^{-1}\,K^{-1}$ for GGST, and further to 0.8 $W\,m^{-1}\,K^{-1}$ for GGSTN. This demonstrates the significant effect of Ge-enrichment and N-doping. Additionally, the temperature dependence of thermal conductivity shows a decreasing trend, primarily due to Umklapp phonon scattering processes.

We demonstrate the applicability of Raman thermometry as a simultaneous structural and thermal characterization technique for GST. Key structural differences between cubic and trigonal phase occurring in GGST can be identified by observing the respective vibrational modes in Raman spectrum. This dual functionality of Raman thermometry eliminates the need for an additional structural characterization technique. This is key as thermal budget imposed during structural and thermal analysis can vary.

SUPPLEMENTARY MATERIAL

See the supplementary material for additional experimental and simulation details: (1) Calibration coefficients of GGST and GGSTN in their different phase conditions, (2) evaluation of errors for the calculation of thermal conductance, (3) methodology used for evaluating the hotspot temperature, (4) temperature-dependent material properties of materials, and (5) electrical resistivity values used for the evaluation of electronic contribution to thermal conductivity by the Wiedemann–Franz law.

ACKNOWLEDGMENTS

This project has received funding from the ECSEL Joint Undertaking (JU) under Grant Agreement No. 101007321. The JU receives support from the European Union's Horizon 2020 research and innovation programme and France, Belgium, Czech Republic, Germany, Italy, Sweden, Switzerland, Turkey. This project has also received funding from the STMicroelectronics-IEMN common laboratory and is partly supported by the French RENATECH network. The authors would like to thank Roberto Simola, Jury Sandrini, Dominique Vignaud, and Marielle Huve for their contributions to this work.

AUTHOR DECLARATIONS

Conflict of Interest

The authors have no conflicts to disclose.

Author Contributions

Akash Patil: Conceptualization (equal); Data curation (lead); Formal analysis (lead); Investigation (equal); Methodology (equal); Visualization (equal); Writing – original draft (lead); Writing – review & editing (equal). **Yannick Le-Friec:** Investigation (equal); Resources (equal). **Pascal Roussel:** Data curation (equal); Formal analysis (equal); Investigation (equal). **Yves Deblock:** Investigation (equal). **Simon Jeannot:** Funding acquisition (equal); Project administration (equal); Supervision (equal). **Philippe Boivin:** Conceptualization (equal); Funding acquisition (equal); Project administration (equal); Supervision (equal). **Emmanuel Dubois:** Project administration (equal); Resources (equal); Writing – review & editing (equal). **Jean-François Robillard:** Conceptualization (equal); Formal analysis (equal); Funding acquisition (equal); Project administration (equal); Resources (equal); Supervision (equal); Validation (lead); Visualization (equal); Writing – review & editing (equal).

DATA AVAILABILITY

The data that support the findings of this study are available from the corresponding author upon reasonable request.

REFERENCES

[1]M. Wuttig and N. Yamada, "Phase-change materials for rewriteable data storage," Nat. Mater. **6**(11), 824–832 (2007).
[2]G. W. Burr, M. J. Breitwisch, M. Franceschini, D. Garetto, K. Gopalakrishnan, B. Jackson, B. Kurdi, C. Lam, L. A. Lastras, A. Padilla, B. Rajendran, S. Raoux, and R. S. Shenoy, "Phase change memory technology," J. Vac. Sci. Technol. B **28**(2), 223–262 (2010).
[3]D. Ielmini and A. L. Lacaita, "Phase change materials in non-volatile storage," Mater. Today **14**(12), 600–607 (2011).
[4]E. Liu, "Materials and designs of magnetic tunnel junctions with perpendicular magnetic anisotropy for high-density memory applications," IIOimport (2018).
[5]S. W. Fong, C. M. Neumann, and H.-S. P. Wong, "Phase-change memory—Towards a storage-class memory," IEEE Trans. Electron Devices **64**(11), 4374–4385 (2017).
[6]H.-Y. Cheng, F. Carta, W.-C. Chien, H.-L. Lung, and M. J. BrightSky, "3D cross-point phase-change memory for storage-class memory," J. Phys. D: Appl. Phys. **52**(47), 473002 (2019).
[7]F. Arnaud, P. Zuliani, J. P. Reynard, A. Gandolfo, F. Disegni, P. Mattavelli, E. Gomiero, G. Samanni, C. Jahan, R. Berthelon, O. Weber, E. Richard, V. Barral, A. Villaret, S. Kohler, J. C. Grenier, R. Ranica, C. Gallon, A. Souhaite, D. Ristoiu, L. Favennec, V. Caubet, S. Delmedico, N. Cherault, R. Beneyton, S. Chouteau, P. O. Sassoulas, A. Vernhet, Y. Le Friec, F. Domengie, L. Scotti, D. Pacelli, J. L. Ogier, F. Boucard, S. Lagrasta, D. Benoit, L. Clement, P. Boivin, P. Ferreira, R. Annunziata, and P. Cappelletti, "Truly innovative 28 nm FDSOI technology for automotive micro-controller applications embedding 16MB phase change memory," in *2018 IEEE International Electron Devices Meeting (IEDM)* (IEEE, 2018), pp. 18.4.1–18.4.4.
[8]N. Yamada, E. Ohno, N. Akahira, K. Nishiuchi, K. Nagata, and M. Takao, "High speed overwritable phase change optical disk material," Jpn. J. Appl. Phys. **26**(S4), 61 (1987).
[9]P. Cappelletti, R. Annunziata, F. Arnaud, F. Disegni, A. Maurelli, and P. Zuliani, "Phase change memory for automotive grade embedded NVM applications," J. Phys. D: Appl. Phys. **53**(19), 193002 (2020).
[10]A. Redaelli, E. Petroni, and R. Annunziata, "Material and process engineering challenges in Ge-rich GST for embedded PCM," Mater. Sci. Semicond. Process. **137**, 106184 (2022).
[11]G. Navarro, G. Bourgeois, J. Kluge, A. L. Serra, A. Verdy, J. Garrione, M.-C. Cyrille, N. Bernier, A. Jannaud, C. Sabbione, M. Bernard, E. Nolot, F. Fillot, P. Noe, L. Fellouh, G. Rodriguez, V. Beugin, O. Cueto, N. Castellani, J. Coignus, V. Delaye, C. Socquet-Clerc, T. Magis, C. Boixaderas, S. Barnola, and E. Nowak, "Phase-change memory: Performance, roles and challenges," in *2018 IEEE International Memory Workshop (IMW)* (IEEE, 2018), pp. 1–4.
[12]H. Y. Cheng, J. Y. Wu, R. Cheek, S. Raoux, M. BrightSky, D. Garbin, S. Kim, T. H. Hsu, Y. Zhu, E. K. Lai, E. Joseph, A. Schrott, S. C. Lai, A. Ray, H. L. Lung, and C. Lam, "A thermally robust phase change memory by engineering the Ge/N concentration in $(Ge, N)_xSb_yTe_z$ phase change material," in *2012 International Electron Devices Meeting* (IEEE, 2012), pp. 31.1.1–31.1.4.
[13]H. Y. Cheng, T. H. Hsu, S. Raoux, J. Y. Wu, P. Y. Du, M. Breitwisch, Y. Zhu, E. K. Lai, E. Joseph, S. Mittal, R. Cheek, A. Schrott, S. C. Lai, H. L. Lung, and C. Lam, "A high performance phase change memory with fast switching speed and high temperature retention by engineering the $Ge_xSb_yTe_z$ phase change material," in *2011 International Electron Devices Meeting* (IEEE, 2011), p. 3.4.1–3.4.4.
[14]G. Navarro, M. Coué, A. Kiouseloglou, P. Noé, F. Fillot, V. Delaye, A. Persico, A. Roule, M. Bernard, C. Sabbione, D. Blachier, V. Sousa, L. Perniola, S. Maitrejean, A. Cabrini, G. Torelli, P. Zuliani, R. Annunziata, E. Palumbo, M. Borghi, G. Reimbold, and B. De Salvo, "Trade-off between SET and data retention performance thanks to innovative materials for phase-change memory," in *2013 IEEE International Electron Devices Meeting* (IEEE, 2013), pp. 21.5.1–21.5.4.
[15]P. Zuliani, E. Varesi, E. Palumbo, M. Borghi, I. Tortorelli, D. Erbetta, G. D. Libera, N. Pessina, A. Gandolfo, C. Prelini, L. Ravazzi, and R. Annunziata, "Overcoming temperature limitations in phase change memories with optimized $Ge_xSb_yTe_z$," IEEE Trans. Electron Devices **60**(12), 4020–4026 (2013).
[16]M. A. Luong, M. Agati, N. Ratel Ramond, J. Grisolia, Y. Le Friec, D. Benoit, and A. Claverie, "On some unique specificities of Ge-rich GeSbTe phase-change material alloys for nonvolatile embedded-memory applications," Phys. Status Solidi RRL **15**(3), 2000471 (2021).
[17]M. A. Luong, N. Cherkashin, B. Pecassou, C. Sabbione, F. Mazen, and A. Claverie, "Effect of nitrogen doping on the crystallization kinetics of $Ge_2Sb_2Te_5$," Nanomaterials **11**(7), 1729 (2021).
[18]S. M. Sadeghipour, L. Pileggi, and M. Asheghi, "Phase change random access memory, thermal analysis," in *Thermal and Thermomechanical Proceedings 10th Intersociety Conference on Phenomena in Electronics Systems, 2006. ITHERM 2006* (IEEE, 2006), pp. 660–665.
[19]V. Giraud, J. Cluzel, V. Sousa, A. Jacquot, A. Dauscher, B. Lenoir, H. Scherrer, and S. Romer, "Thermal characterization and analysis of phase change random access memory," J. Appl. Phys. **98**(1), 013520 (2005).
[20]H.-K. Lyeo, D. G. Cahill, B.-S. Lee, J. R. Abelson, M.-H. Kwon, K.-B. Kim, S. G. Bishop, and B. Cheong, "Thermal conductivity of phase-change material $Ge_2Sb_2Te_5$," Appl. Phys. Lett. **89**(15), 151904 (2006).

[21]J. P. Reifenberg, M. A. Panzer, S. Kim, A. M. Gibby, Y. Zhang, S. Wong, H.-S. P. Wong, E. Pop, and K. E. Goodson, "Thickness and stoichiometry dependence of the thermal conductivity of GeSbTe films," Appl. Phys. Lett. **91**(11), 111904 (2007).
[22]M. Kuwahara, O. Suzuki, Y. Yamakawa, N. Taketoshi, T. Yagi, P. Fons, T. Fukaya, J. Tominaga, and T. Baba, "Temperature dependence of the thermal properties of optical memory materials," Jpn. J. Appl. Phys. **46**(6S), 3909 (2007).
[23]W. P. Risk, C. T. Rettner, and S. Raoux, "*In situ* 3ω techniques for measuring thermal conductivity of phase-change materials," Rev. Sci. Instrum. **79**(2), 026108 (2008).
[24]E. Bozorg-Grayeli, J. P. Reifenberg, K. W. Chang, M. Panzer, and K. E. Goodson, "Thermal conductivity and boundary resistance measurements of GeSbTe and electrode materials using nanosecond thermoreflectance," in *2010 12th IEEE Intersociety Conference on Thermal and Thermomechanical Phenomena in Electronic Systems* (IEEE, 2010), pp. 1–7.
[25]J.-L. Battaglia, A. Cappella, E. Varesi, V. Schick, A. Kusiak, C. Wiemer, M. longo, A. Gotti, and B. Hay, "Temperature-dependent thermal characterization of $Ge_2Sb_2Te_5$ and related interfaces by the photothermal radiometry technique," J. Phys.: Conf. Ser. **214**(1), 012102 (2010).
[26]K. S. Siegert, F. R. L. Lange, E. R. Sittner, H. Volker, C. Schlockermann, T. Siegrist, and M. Wuttig, "Impact of vacancy ordering on thermal transport in crystalline phase-change materials," Rep. Prog. Phys. **78**(1), 013001 (2015).
[27]E. A. Scott, E. Ziade, C. B. Saltonstall, A. E. McDonald, M. A. Rodriguez, P. E. Hopkins, T. E. Beechem, and D. P. Adams, "Thermal conductivity of $(Ge_2Sb_2Te_5)_{1-x}C_x$ phase change films," J. Appl. Phys. **128**(15), 155106 (2020).
[28]Q. Li, O. Levit, E. Yalon, and B. Sun, "Temperature-dependent thermal conductivity of $Ge_2Sb_2Te_5$ polymorphs from 80 to 500 K," J. Appl. Phys. **133**(13), 135105 (2023).
[29]J.-L. Battaglia, A. Kusiak, and K. Ghosh, "The use of photothermal techniques for thermal conductivity and thermal boundary resistance measurements of phase-change chalcogenides alloys," J. Appl. Phys. **129**(5), 055106 (2021).
[30]E. Gemo, S. V. Kesava, C. R. De Galarreta, L. Trimby, S. García-Cuevas Carrillo, M. Riede, A. Baldycheva, A. Alexeev, and C. D. Wright, "Simple technique for determining the refractive index of phase-change materials using near-infrared reflectometry," Opt. Mater. Express **10**(7), 1675 (2020).
[31]W. H. P. Pernice and H. Bhaskaran, "Photonic non-volatile memories using phase change materials," Appl. Phys. Lett. **101**(17), 171101 (2012).
[32]D. N. Wright, E. S. Marstein, A. Rognmo, and A. Holt, "Plasma-enhanced chemical vapour-deposited silicon nitride films; The effect of annealing on optical properties and etch rates," Sol. Energy Mater. Sol. Cells **92**(9), 1091–1098 (2008).
[33]T. Beechem, S. Graham, S. P. Kearney, L. M. Phinney, and J. R. Serrano, "Invited article: Simultaneous mapping of temperature and stress in microdevices using micro-Raman spectroscopy," Rev. Sci. Instrum. **78**(6), 061301 (2007).
[34]T. Batten, A. Manoi, M. J. Uren, T. Martin, and M. Kuball, "Temperature analysis of AlGaN/GaN based devices using photoluminescence spectroscopy: Challenges and comparison to Raman thermography," J. Appl. Phys. **107**(7), 074502 (2010).
[35]M. Kuball and J. W. Pomeroy, "A review of Raman thermography for electronic and opto-electronic device measurement with submicron spatial and nanosecond temporal resolution," IEEE Trans. Device Mater. Reliab. **16**(4), 667–684 (2016).
[36]I. Calizo, A. A. Balandin, W. Bao, F. Miao, and C. N. Lau, "Temperature dependence of the Raman spectra of graphene and graphene multilayers," Nano Lett. **7**(9), 2645–2649 (2007).
[37]K. S. Andrikopoulos, S. N. Yannopoulos, A. V. Kolobov, P. Fons, and J. Tominaga, "Raman scattering study of GeTe and $Ge_2Sb_2Te_5$ phase-change materials," J. Phys. Chem. Solids **68**(5), 1074–1078 (2007).
[38]P. Němec, V. Nazabal, A. Moreac, J. Gutwirth, L. Beneš, and M. Frumar, "Amorphous and crystallized Ge–Sb–Te thin films deposited by pulsed laser: Local structure using Raman scattering spectroscopy," Mater. Chem. Phys. **136**(2), 935–941 (2012).
[39]K. S. Andrikopoulos, S. N. Yannopoulos, G. A. Voyiatzis, A. V. Kolobov, M. Ribes, and J. Tominaga, "Raman scattering study of the a-GeTe structure and possible mechanism for the amorphous to crystal transition," J. Phys.: Condens. Matter **18**(3), 965–979 (2006).
[40]R. Mazzarello, S. Caravati, S. Angioletti-Uberti, M. Bernasconi, and M. Parrinello, "Signature of tetrahedral Ge in the Raman spectrum of amorphous phase-change materials," Phys. Rev. Lett. **104**(8), 085503 (2010).
[41]M. Bouška, S. Pechev, Q. Simon, R. Boidin, V. Nazabal, J. Gutwirth, E. Baudet, and P. Němec, "Pulsed laser deposited GeTe-rich GeTe-Sb_2Te_3 thin films," Sci. Rep. **6**(1), 26552 (2016).
[42]P. Kazimierski, J. Tyczkowski, M. Kozanecki, Y. Hatanaka, and T. Aoki, "Transition from amorphous semiconductor to amorphous insulator in hydrogenated carbon–germanium films investigated by Raman spectroscopy," Chem. Mater. **14**(11), 4694–4701 (2002).
[43]A. R. Zanatta, I. Chambouleyron, and P. V. Santos, "Study of structural changes in amorphous germanium–nitrogen alloys by optical techniques," J. Appl. Phys. **79**(1), 433–438 (1996).
[44]M. Lax, "Temperature rise induced by a laser beam," J. Appl. Phys. **48**(9), 3919–3924 (1977).
[45]B. Stoib, S. Filser, J. Stötzel, A. Greppmair, N. Petermann, H. Wiggers, G. Schierning, M. Stutzmann, and M. S. Brandt, "Spatially resolved determination of thermal conductivity by Raman spectroscopy," Semicond. Sci. Technol. **29**(12), 124005 (2014).
[46]A. L. Serra, G. Bourgeois, M. C. Cyrille, J. Cluzel, J. Garrione, G. Navarro, and E. Nowak, "Optimization of 3ω method for phase-change materials thermal conductivity measurement at high temperature," in *2019 IEEE 32nd International Conference on Microelectronic Test Structures (ICMTS)* (IEEE, 2019), pp. 76–79.
[47]E. Bozorg-Grayeli, J. P. Reifenberg, M. A. Panzer, J. A. Rowlette, and K. E. Goodson, "Temperature-dependent thermal properties of phase-change memory electrode materials," IEEE Electron Device Lett. **32**(9), 1281–1283 (2011).
[48]A. Kusiak, C. Chassain, A. M. Canseco, K. Ghosh, M.-C. Cyrille, A. L. Serra, G. Navarro, M. Bernard, N.-P. Tran, and J.-L. Battaglia, "Temperature-dependent thermal conductivity and interfacial resistance of Ge-rich $Ge_2Sb_2Te_5$ films and multilayers," Phys. Status Solidi RRL **16**(4), 2100507 (2022).
[49]C. Chassain, A. Kusiak, C. Gaborieau, Y. Anguy, N.-P. Tran, C. Sabbione, M.-C. Cyrille, C. Wiemer, A. Lamperti, and J.-L. Battaglia, "Thermal characterization of Ge-rich GST/TiN thin multilayers for phase change memories," J. Appl. Phys. **133**(22), 225102 (2023).
[50]D. G. Cahill and R. O. Pohl, "Lattice vibrations and heat transport in crystals and glasses," Annu. Rev. Phys. Chem. **39**(1), 93–121 (1988).
[51]J. Lee, E. Bozorg-Grayeli, S. Kim, M. Asheghi, H.-S. Philip Wong, and K. E. Goodson, "Phonon and electron transport through $Ge_2Sb_2Te_5$ films and interfaces bounded by metals," Appl. Phys. Lett. **102**(19), 191911 (2013).